

The Computation of Wind Speed and Wave Heights From Geos 3 Data

NELLY MOGNARD AND BERNARD LAGO

Groupe de Recherches de Géodésie Spatiale, Centre National d'Etudes Spatiales, 31055 Toulouse Cedex, France

We have processed radar altimeter data from more than 100 Geos 3 passes. The statistical analysis of the stretching of the leading edge of the return radar pulses gives us an estimate of the significant wave heights, as reported by other scientists. Moreover, the automatic gain control level measurements of the reflected power provide an evaluation of the wind speed. The wave height and wind speed estimates are in favorable agreement with the meteorological information obtained from weather maps used as sea truth, thus resulting in interesting complementarities.

1. INTRODUCTION

The low-orbiting NASA satellite Geos 3, launched on April 9, 1975, is equipped with a radar altimeter working at a 13.9-GHz frequency. Radar pulses of 12.5-ns width probe the ocean surface at a pulse repetition frequency of 100 pulses per second. One of the major objectives of the Geos 3 mission is to demonstrate the radar altimeter's ability to monitor sea state. Using the sampling of the average wave forms of the return pulses, studies were undertaken to determine or improve $H1/3$ computations [Rufenach and Alpers, 1978; Gower, 1978; Fedor and Barrick, 1978].

Our purpose is to point out that sea state information can be deduced from the automatic gain control (AGC) variations as well as from the $H1/3$ computation. The AGC level is a measurement of the reflected power and supplies indications of the instantaneous wind speed along the satellite track, whereas a statistical analysis of the stretching of the return pulse leading edge gives an estimation of the mean wave heights ($H1/3$).

These two measured quantities appear to have a complementary behavior in terms of sea state. The $H1/3$ computation gives good results in the regions where the mean wave heights are more than 3 m [Pierson and Salfi, 1978], whereas the AGC sensitivity increases in the regions where the wind velocity is low, such as in anticyclonic regions.

In order to analyze and interpret the altimeter data we need sea truth data along the satellite track. We have used weather maps to derive qualitative and quantitative sea truth data.

After studying more than 100 Geos 3 passes well distributed over the oceans we selected four characteristic satellite passes to analyze with two different approaches. We first compared the altimeter data directly with the meteorological information supplied by the weather maps. We then utilized a theoretical model which forecasts, by means of an empirical formula [Cox and Munk, 1954], the reflected power attenuation due to the surficial wind velocity along the satellite track. These two approaches are in good agreement, indicating that these two measured quantities, when they are used to determine sea state variations, complement each other.

2. THE STRETCHING OF THE RETURN PULSES AND THE CORRESPONDING $H1/3$ EVALUATION

We intend to determine significant wave heights through their dependence on the mean wave shapes received by the altimeter. The stretching of the leading edge of the return pulses due to changes in ocean surface roughness is the physical phenomenon used to deduce $H1/3$ values. The backscattered signal from the oceanic surface is square law detected

and then point sampled by 16 wave form sampling gates, each 12.5 ns wide and spaced 6.25 ns apart. The fluctuating received wave form requires that a large number of individual wave forms must be averaged in order to estimate the ensemble mean wave form [Miller *et al.*, 1972]. Average wave forms, using an averaging time of 2 s, are performed on board the satellite by means of these 16 sampling gates.

The mean return wave form for a short-pulse altimeter operating at nadir is conceptually affected by the contribution of the altimeter system point target impulse response, the sea surface impulse response, and the tracking loop jitter effect [McGoogan, 1975]. The sea surface impulse response depends on the sea surface roughness, that is, on the wave heights. When the wave heights along the satellite track are significant, the backscattered power reflected from the rough oceanic surface returns from differing depths, which thus creates a random stretching of the leading edge of the return pulse. The determination of this stretching, by means of a statistical analysis, provides a measurement of the significant wave heights.

We have assumed, as is usual for this kind of analysis, that the different contributions to the mean wave form can be reasonably approximated by Gaussian functions [Miller and Hayne, 1972] and that the pointing angle errors have a negligible effect on modeling the leading edge of the return wave form [Hayne, 1977]. The sea surface impulse response can be approximated mathematically by the product of the convolution of the flat sea impulse response onto the wave height probability density function. With the above assumptions the generalized expression for return power as a function of time can be reduced to an error function formula with mathematical ease which is, in fact, the integrated Gaussian obtained as a result of the convolution product of Gaussian functions of time.

The resultant function of time is, for our purposes, fully characterized by its variance σ^2 , which can be expressed as a sum of the variances of the contributing functions of time involved:

$$\sigma^2 = \sigma_0^2 + \sigma_j^2 + \sigma_s^2 \quad (1)$$

where σ_0^2 is the variance of the transmitted pulse shape, σ_j^2 is the variance of the tracking loop jitter, and σ_s^2 is the variance of the wave height probability density function. In this expression, the physically interesting quantity is σ_s ; for us, σ_j and σ_0 represent perturbations which can be thus approximated while only contributing slightly to the limiting accuracy. We have used $\sigma_j = 4$ ns and $\sigma_0 = 6.35$ ns.

A significant wave height value ($H1/3$) can be related to σ_s [Longuet-Higgins, 1952]:

$$H1/3 = 4\sigma_s \text{ m} \quad (2)$$

If we use the variances expressed in nanoseconds, we obtain the relation

$$H1/3 = 0.6(\sigma^2 - \sigma_0^2 - \sigma_f^2)^{1/2} \quad (3)$$

To compute the variance deduced from the slope of the average wave form leading edge, we may fit the measured average signal directly to an error function in a least squares sense or fit its derivative to a Gaussian function [Gower, 1978]. We have used the second method, since it was more convenient for

us and yields results similar to the first one. A comparison of the two methods can be made by utilizing our plotted $H1/3$ computations (see Figure 1c) and the results obtained by Rufenach and Alpers, who have processed the same data for the pass taken during the North Atlantic storm, using the first mathematical method mentioned above [Rufenach and Alpers, 1978].

Using this method, we have computed significant wave heights over a distance of about 22 km, which corresponds to

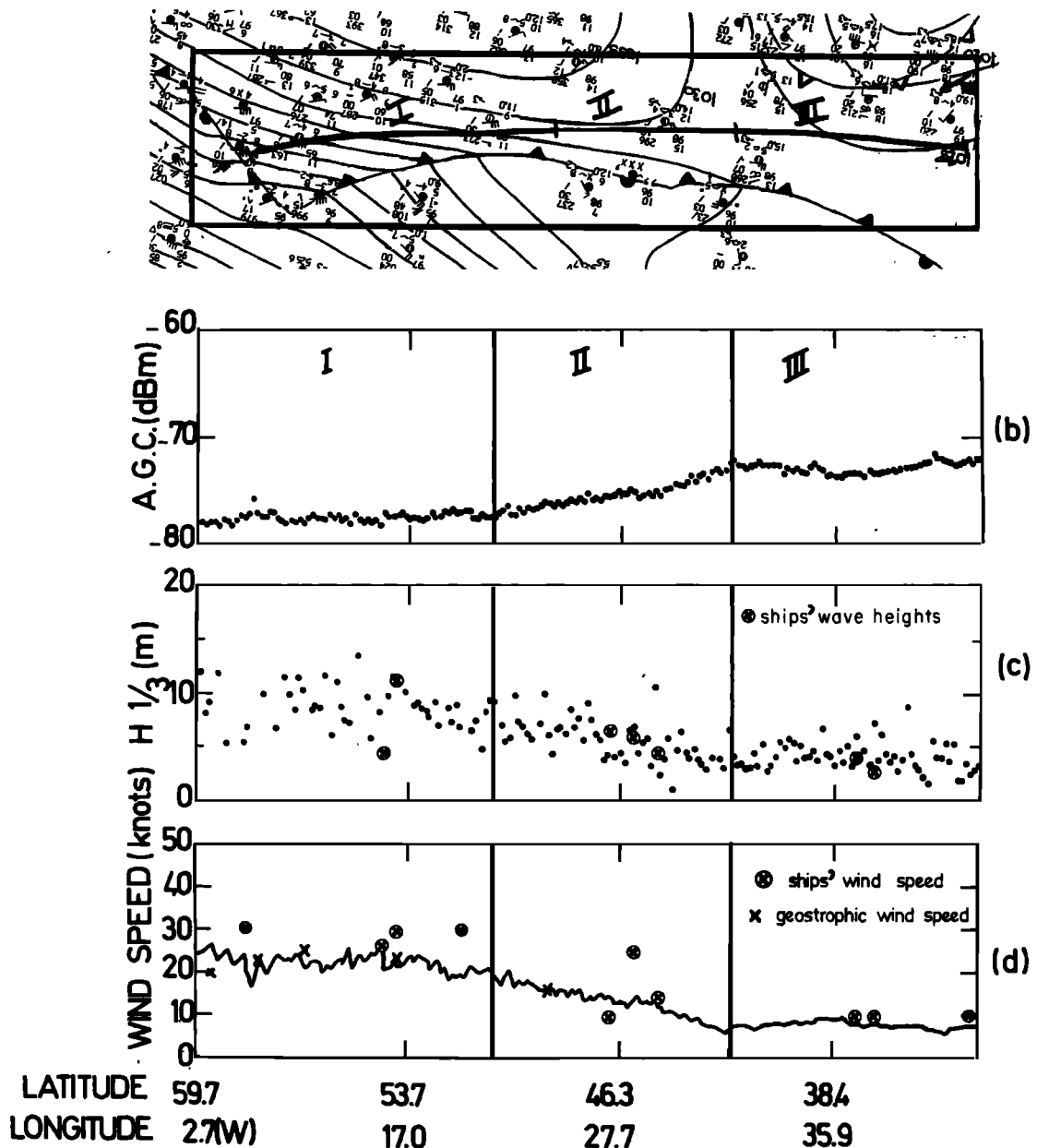


Fig. 1. North Atlantic pass from ENE to WSW on February 25, 1976, at 0800 UT drawn on a weather map for the same day at 1200 UT. The first part of the pass crosses a stormy region where winds of 25-30 kn have been blowing for 2 days and where the waves are fully or nearly fully developed. This was deduced by examining successive weather maps. Note the high $H1/3$ values and low AGC values. In the second part the sea state becomes progressively quieter with a simultaneous AGC increase and $H1/3$ decrease. The third part is a very quiet region with nearly constant high values of AGC and low values of $H1/3$. In Figures 1-4 for each selected pass we show the following data. (a) A weather map corresponding to the data closest to the occurrence of the satellite track. The parts of the pass characterized by a meteorological situation are limited by dashes. (b) The AGC data. (c) The $H1/3$ curve, obtained by a Gaussian fit to the derivative of the leading edge of the averaged altimeter output as a function of time (see section 2). On the same graph we have plotted (crosses inside circles) $H1/3$ deduced from the ship's measurements. (d) The wind speed, deduced from AGC data by using the Cox and Munk formula (see section 3). On the same graph we have plotted (crosses inside circles) wind speed from each weather ship.

the distance that the satellite travels in 3.2 s (sampling time interval for the mean wave forms for the high data rate mode). For the different Geos 3 passes we have obtained $H1/3$ values that we have plotted (curve c) for each case. On the same curve c we have plotted (cross inside circle) $H1/3$ data taken from the weather maps of ships at the nearest approach, deducing $H1/3$ from the reported swell and wind wave heights.

Comparison of Geos 3 significant wave height with National Data Buoy has been made by using a similar technique to compute $H1/3$ [McMillan and Roy, 1977]. The authors concluded that the satellite-derived estimate of $H1/3$ was accurate to about 55 cm.

3. THE AGC VARIATION AND THE CORRESPONDING EVALUATION OF WIND SPEED

A receiver automatic gain control is used on Geos 3 to normalize the mean detected return pulses for acquisition and tracking. The sampling of the resultant video signal is performed every 0.1 s and supplies a measurement of the reflected power P_r :

$$\text{AGC(dBm)} = 10 \log_{10} (P_r/P_0)$$

where P_0 has a value of 1 mW and is taken as a reference power.

For tracking, the AGC control signal is derived from the tracking plateau gate output. The receiver gain is adjusted to hold an average of the plateau gate outputs (over about 10 pulses) equal to a constant [Leitao et al., 1974]. We have plotted the AGC data on curve b with an averaged point for each 3.2 s.

At a 13.9-GHz frequency, one considers that the atmospheric attenuation can usually be ignored for all but a few notable exceptions [Skolnik, 1970; Brown, 1977]. The cases of heavy rainfalls will be examined when we deal with the meteorological considerations. In the following computations the atmospheric attenuation is, as usual, not taken into account.

The average received power P_r can be expressed in terms of the transmitted power P_t , the antenna gain G_t , the operating wavelength λ , the range R of the target, the sea surface in our case, and the sea surface scattering cross section per unit area σ_0 .

$$P_r = \frac{\lambda^2}{(4\pi)^3} \int_{\text{illuminated area}} \frac{P_t G_t^2 \sigma_0}{R^4} dA \quad (4)$$

The scattering cross section σ_0 can be expressed, for the specular point model, where the sea surface slopes are nearly Gaussian and isotropic in their distribution by [Barrick, 1974; Hammond et al., 1977]

$$\sigma_0 = (|R(0)|^2/S^2) \sec^4 \theta \exp [-(\tan^2 \theta)/S^2] \quad (5)$$

where θ is the angle of incidence and $R(0)$ is the Fresnel reflection coefficient of the air-to-surface interface at normal incidence. This coefficient varies only from about -2.08 to -2.37 dB at 13.9 GHz for extreme variations in water temperature and salinity [Matthews, 1975].

An empirical relationship between the averaged upwind/crosswind mean square slope S^2 and wind speed has been obtained [Cox and Munk, 1954]:

$$S^2 = \alpha + \beta U(\text{m/s}) \quad (6)$$

where $\alpha = 0.003$, $\beta = 0.00512$, and U is the averaged wind speed in meters per second, measured at 12.5 m above sea level.

In our case, θ is small, certainly smaller than 2.6° , the angle

of the antenna beam width for an attenuation of 3 dBm. This makes it possible to set $\theta = 0$ in (5) without significant error. Thus

$$\sigma_0 = |R(0)|^2/(\alpha + \beta U) \quad (7)$$

As soon as the trailing edge of the incident pulse has reached the sea surface, the reflected power may be expressed by

$$P_r \approx \frac{\lambda^2}{(4\pi)^3} \frac{P_t G_t^2}{h^4} \sigma_0(\theta = 0) A \quad (8)$$

where h is the Geos 3 altitude and A is the illuminated area easily expressed by $'2\pi h c \delta'$, where δ is the duration of the transmitted signal and c is the light velocity.

By using (7) and (8), the automatic gain control is directly related to the wind speed. However, variations in the satellite pointing angle from nadir up to 0.8° have been often noted. These variations produce drops in the received power which induce an artificial enhancement in the wind speed estimation especially for winds higher than 20 kn (1 kn = 0.5 m/s). We have therefore corrected the data for pointing angle errors according to the scheme given by Brown and Curry [1977]. We then obtain the following relationship:

$$S = \text{AGC}_c - 10 \log_{10} \frac{P_t}{P_0} - 10 \log_{10} \frac{\lambda^2 G_t^2 A}{(4\pi)^3 h^4} \quad (9)$$

where $S = 10 \log_{10} \sigma_0$ and AGC_c is the automatic gain control value after correction due to the pointing angle errors. The wind speed is then given by

$$U(\text{m/s}) = \frac{1}{\beta} \left(\frac{|R(0)|^2}{10^{S/10}} - \alpha \right) \quad (10)$$

For easy comparison with ships' data given on the weather maps we have computed the wind speed in knots:

$$U(\text{kn}) = \vartheta \left(\frac{|R(0)|^2}{10^{S/10}} - \alpha \right) \quad (11)$$

where $\vartheta = 1.9456/\beta$.

For each selected pass we have plotted AGC data on curve b and the corresponding $U(\text{kn})$ given by (11) on curve d .

On the same curve are plotted (crosses) our computed geostrophic wind speed at each occurrence of a middle point between successive isobars. For obvious reasons, no such evaluation can be found near anticyclonic and depression centers or in the cols.

Moreover, on the same curve d we have plotted (cross inside circle) explicit wind speed data taken from the maps of weather ships at the nearest approach.

4. DATA PROCESSING AND ANALYSIS OF THE RESULTS

As was mentioned before, we have processed more than 100 Geos 3 passes distributed over most of the oceans and have found favorable agreement between the significant wave heights, the AGC data, and the AGC-deduced wind speed on the one hand and information deduced from the weather maps on the other. (The latter includes the localization of meteorological features (anticyclonic centers, depression centers, and storms), the geostrophic wind speed evaluation, and weather ship data.)

To illustrate these results so as to provide a justification for some of our conclusions, we have selected four cases chosen for their diverse meteorological situations as well as for the proximity of the satellite tracks. The reader will find the char-

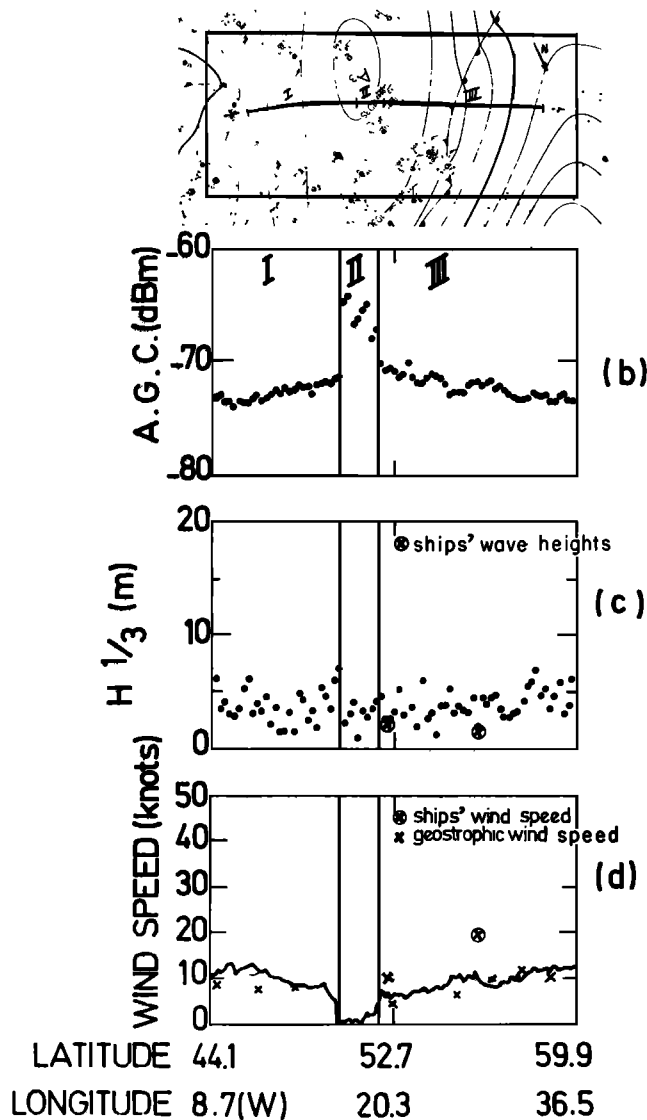


Fig. 2. North Atlantic pass from SE to NW on April 23, 1975, at 0300 UT drawn on a weather map for the same day at 0600 UT. The pass crosses an anticyclone near its center. Note the sharp and narrow AGC increase located near the center of the anticyclone in contrast with the smooth behavior of the $H_{1/3}$ curve. See Figure 1 caption for an explanation of the parts of the figure.

acteristics of each pass in the figure legends. We will now present our general verifications and related comments pertaining to the following three items: (1) $H_{1/3}$ analysis, (2) AGC analysis, and (3) AGC-deduced wind speed analysis and comparisons with the other wind speed data.

$H_{1/3}$ Analysis (Curves c)

We ascertain high $H_{1/3}$ values in the regions where the waves are fully developed, particularly in the storms (part I of Figure 1 and part I of Figure 3) where winds of about 30 kn have been blowing for 2 days. We note the progressive decrease of $H_{1/3}$ values with the diminution of atmospheric pressure gradient (part II of Figure 1). We also note the proper order of magnitude of the computed $H_{1/3}$ values, all distributed between 0 and about 10 m.

The $H_{1/3}$ values are noisy, but mean variations are smooth (Figures 1–4). Outside the storm regions the behavior is also smooth, but moreover, in quiet regions it is very difficult to see

any variation (Figure 2). For low wave heights with values of the order of 3 m or less the effect of the variability of the tracking loop jitter σ , is not negligible, and the accuracy of the $H_{1/3}$ determination decreases [Pierson and Salfi, 1978]. However, for each satellite pass (Figures 1–4) the comparison with the data reported by the ships and plotted on the weather maps shows a good agreement.

AGC Analysis (Curves b)

According to the logarithmic expression relating AGC variations to wind speed, we ascertain very high AGC values in the anticyclonic centers (part II of Figure 2 and part IV of Figure 3) and high values in regions of atmospheric cols (part III of Figure 4).

On the other hand, we usually see small AGC values in regions where variation in the atmospheric pressure gradients occurs (parts II and III of Figure 1; parts I and III of Figure 2; parts II, III, and V of Figure 3; and parts I, II, and IV of Figure 4) and even very small values in the stormy regions (part I of Figure 1 and part I of Figure 3).

A sharp AGC increase at the beginning and decrease at the end of the anticyclonic center is evident (part IV of Figure 3). The same sort of behavior (part II of Figure 2) is not located exactly in the central part of the anticyclone. This geographical translation can be explained by a time interval of 3 hours between the weather map observations and the satellite crossing. This characteristic AGC behavior is in contrast with the smooth behavior of $H_{1/3}$ (Figure 2) as formerly noticed.

Generally, we note rather small noise (less than 2 dBm) for the AGC values but a noise increase (to 3–4 dBm) for the high AGC values. This noise, which we have not represented on the curves, has little or no effect on the AGC-deduced wind speed because of its exponential behavior, which tends to minimize the effect of noise on wind speed evaluation for high AGC values.

AGC-Deduced Wind Speed Analysis, Comparison With the Other Wind Speed Data (Curves d) and Accuracy of the Wind Measurement

The examination of curves *d* (Figures 1 and 2) shows a good agreement between AGC-deduced wind speed (U_{AGC}) and the wind speed used as sea truth data, as well as between geostrophic wind speed (U_{gsp}) and ship-observed wind speed (U_{ship}). However, for the cases represented in Figures 3 and 4 the agreement is rather poor. If we examine numerous Geos 3 passes, it appears that this poor agreement is exceptional, as is indicated by a statistical analysis performed over a total of 21 Geos 3 passes.

For this analysis we have grouped the data according to the U_{AGC} values: group *a*, $U_{AGC} < 10$ kn; group *b*, $10 \leq U_{AGC} < 20$ kn; group *c*, $20 \leq U_{AGC} < 30$ kn. For each of the three groups we have computed the values $\Delta U_1 = U_{gsp} - U_{AGC}$ and $\Delta U_2 = U_{ship} - U_{AGC}$ in each interval of 2 kn, and we have grouped the eccentric values in an interval beyond ± 12 kn. The results are plotted in Figure 5, curves *a*, *b*, and *c*.

For line *d* in Figure 5 we have summed the number of occurrences in the interval ± 4 kn centered at zero, and the number of occurrences right and left of this interval. We note the lack of bias between U_{gsp} and U_{AGC} , whereas U_{ship} shows an almost systematic overestimation when compared with the two wind speed calculations.

The lack of bias between U_{AGC} and U_{gsp} , evident for the whole of line *d* and for groups *a* and *b*, is in contrast with group *c*, for which U_{gsp} is slightly underestimated. The U_{AGC}

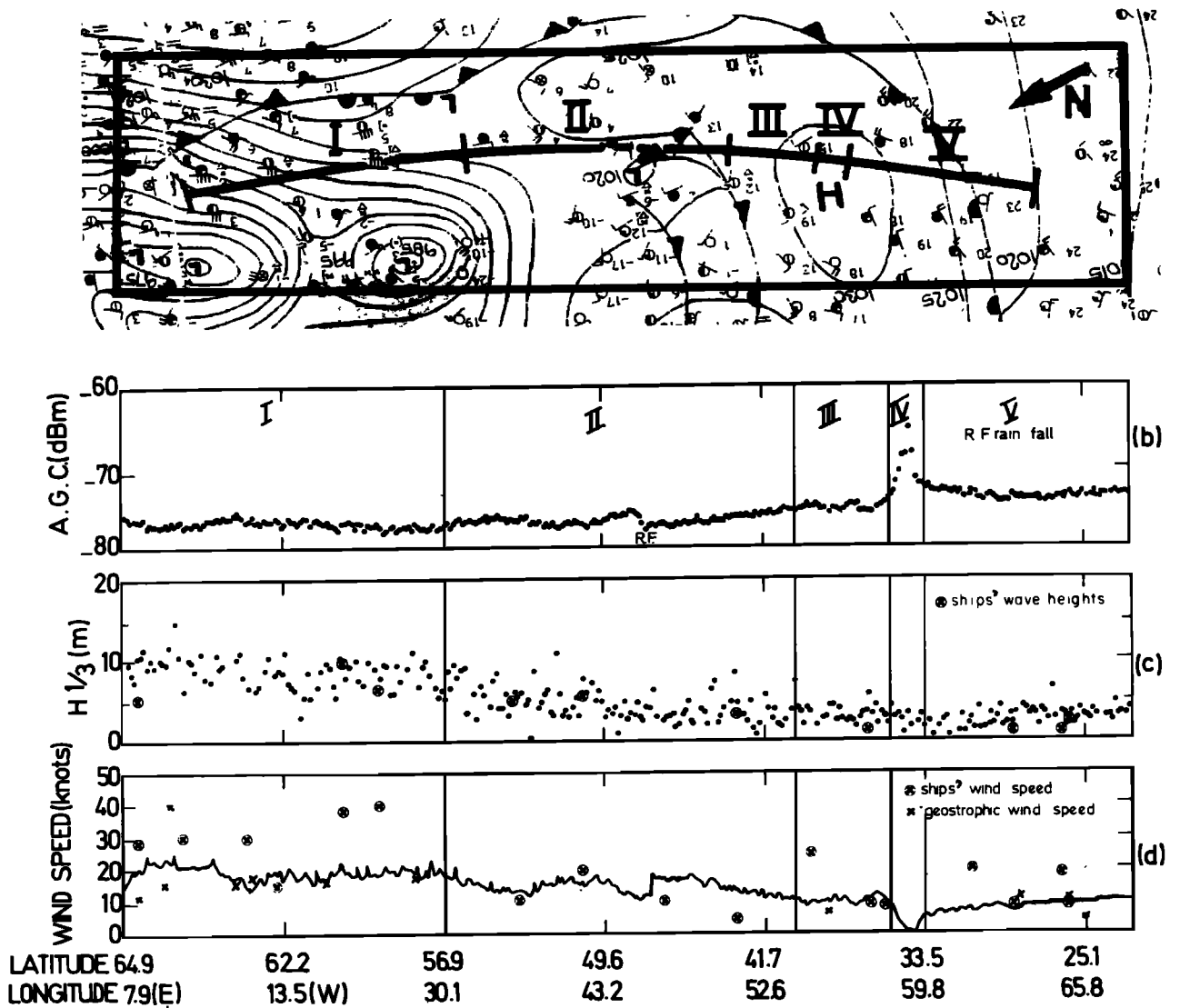


Fig. 3. North Atlantic pass from ENE to WSW occurring on February 26, 1976, at 0900 UT plotted on a weather map drawn up on the same day at 0000 UT. In this pass we are concerned with the evolution 12 hours later of the meteorological situation of pass 1. As before, the satellite track crosses a storm in the first part of the pass with associated high $H_{1/3}$ values and low AGC values. In the second part we observe a progressive decreasing trend of $H_{1/3}$ values when low AGC values remain stable. The explanation may be found in section 5. The third, fourth, and fifth parts occur across quiet regions with low and stable $H_{1/3}$ values while AGC values are high with a sharp and narrow increase located at the center of the anticyclone. See Figure 1 caption for an explanation of the parts of the figure.

evaluation seems to be generally intermediate between the two other determinations.

In Figure 5 we note the presence of some eccentric values contained in the interval beyond 12 kn. The more characteristic eccentric values over the 21 cases considered pertain to the Geos 3 passes represented in Figures 3 and 4. They are located in part I of Figure 3 and part II of Figure 4. In these two cases the quality of our geostrophic evaluation is questionable because of the rapid modification of isobars as suggested by direct comparison with successive weather maps.

For example, in part II of Figure 4 the erratic values have been obtained inside a depression D3 which may be poorly located in relation to the pass because of the time interval between the measurement and the satellite crossing as well as to the rapid evolution of the depression D3 itself.

In order to compare the accuracy of U_{AGC} measurements with a Seasat scatterometer capability of ± 4 kn we have eval-

uated the frequency distribution of our residuals at 1σ , 2σ , and 3σ (Table 1), where $1\sigma = 4$ kn.

If we consider theoretical probabilities deduced from the error function, i.e., 68.27% at 1σ , 95.45% at 2σ , and 99.73% at 3σ , we see that the distribution of ΔU_1 is in close agreement with the theoretical rule. This allows us to conclude an accuracy of 4 kn for U_{AGC} , using U_{GBP} as true reference, which is much the same as the Seasat scatterometer capability (curves a and b). For curve c ($U > 20$ kn) we conclude a greater uncertainty of 5 or 6 kn. As for the ΔU_2 results we indicate an uncertainty of about 6 kn for $U < 20$ kn (curves a and b) and about 8 kn for $U > 20$ kn (curve c).

5. CORRELATIONS $H_{1/3}$ AND AGC-DEDUCED WIND SPEED: METEOROLOGICAL CONSIDERATIONS

In the preceding paragraph we have checked the validity of the two computed quantities, significant wave heights and

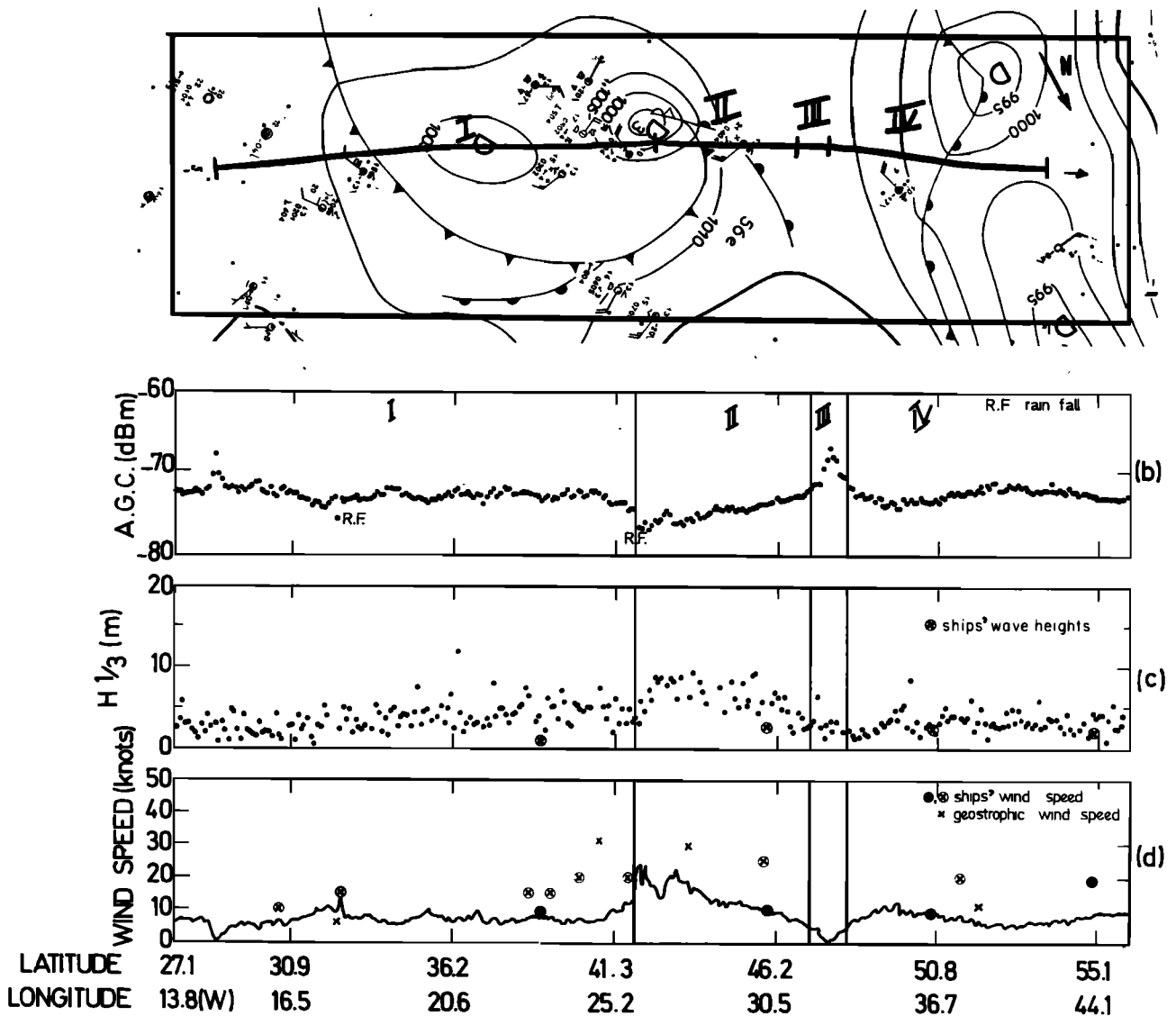


Fig. 4. North Atlantic pass from SE to NW occurring on November 10, 1975, at 0400 UT plotted on a weather map drawn up on the same day at 0600 UT. The pass begins near the African continent and goes on across very localized depressions and atmospheric fronts. It then crosses a meteorological col and ends near a depression region. On curves *c* and *d* have been plotted additional ship measurements (solid circles) made on the same day at 0000 UT. Note the opposite behavior between $H_{1/3}$ and AGC variations for the two zones located in the middle of the track where the reflected power abruptly decreases in the vicinity of the occlusion and abruptly increases at the meteorological col crossing. See Figure 1 caption for an explanation of the parts of the figure.

wind speed, by analyzing Geos 3 data. The degree of confidence in these quantities is limited by the lack of real sea truth data. We are now concerned with the meteorological and oceanographical behavior of these parameters in order to determine when they are correlated and when they are complementary.

In a case of slow meteorological evolution, for example, where the wind has been blowing for 1–2 days, we most likely expect a good correlation between the two quantities. Part I of Figure 1 is a perfect example of this.

Other meteorological situations also produce good correlation between these two quantities, as can be seen in part IV of Figure 4 and, at a smaller scale, in part II of Figure 2.

On the contrary, in a case of rapid meteorological evolution we can expect uncorrelated behavior between wind speed and $H_{1/3}$. This is the case shown in part II of Figure 3, where a depression is rapidly crossing the satellite track, as is con-

firmed by examination of successive weather maps. We observe a decrease in the $H_{1/3}$ curve as soon as part II begins, whereas the wind speed decreases only weakly at the end of part II.

Another example may be illustrated by part II of Figure 2, where the wind speed is almost null, smaller than in the neighboring parts where the $H_{1/3}$ values remain practically constant. It seems to be indicative of a swell propagating from afar as reported on the weather map by a ship. Appreciably small values of $H_{1/3}$ are obtained for the similar case shown by part IV of Figure 3.

A new question can be raised concerning the influence of physical phenomena other than the sea surface effect. If we limit our interest to physical events which contribute more than 2 dBm (for a 13.9-GHz frequency), we can only imagine heavy rainfalls to a depth greater than 1 km. Such an effect most probably concerns a narrow part of the track. Perhaps

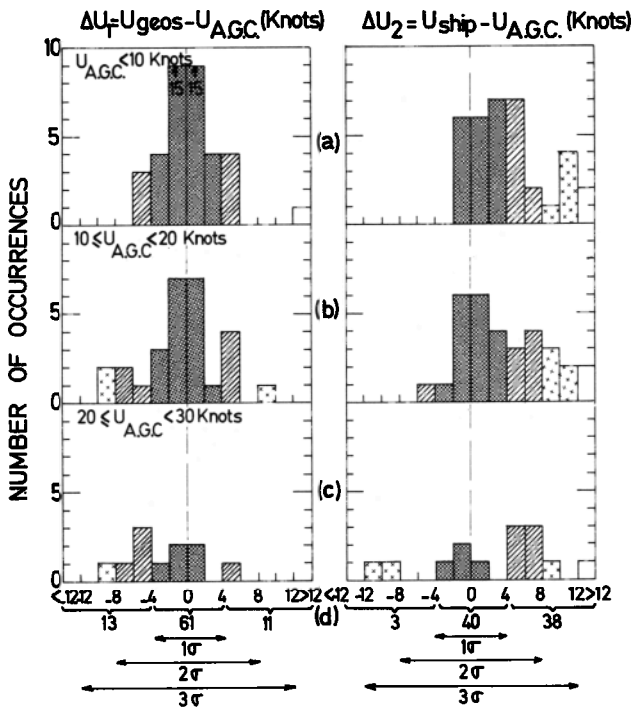


Fig. 5. Histograms of the differences between U_{AGC} and the wind speed geostrophic calculations and between U_{AGC} and the ships' measurements obtained by using 21 Geos 3 passes.

three such occurrences can be seen in our cases (they are indicated on the curves *b* by R. F.), one in the middle of part II of Figure 3, one in the middle of part I, and another at the limit between parts I and II of Figure 4. In these three occurrences, we may be seeing the proximity of meteorological fronts.

6. CONCLUSION

In our paper the principal contribution is mainly the computation of wind speed from AGC data. It must be pointed out that this was possible only because the narrow antenna beam width allowed for the use of Cox and Munk's formulas.

It has been shown that these wind speed measurements meet the Seasat requirement of ± 4 kn for the low wind speed values ($U < 20$ kn) and a little less for the intermediate values ($20 \text{ kn} < U < 30 \text{ kn}$), beyond which there are no measurements.

From the comparison with the weather maps the Geos 3 estimates of both significant wave height and wind speed show

a good agreement with the ground-measured data and geostrophic estimations. Wind speed estimates from Geos 3 data based on the same principle have recently been made [Brown, 1978], and the comparison with NOAA hindcast data shows a good agreement.

It can be expected that measurements of significant wave heights by the Geos 3 satellite radar altimeter can help to construct contour maps of sea state for large regions of the oceans [Parsons, 1976]. The ability of the Geos 3 radar altimeter to sense on a near-real-time basis both significant wave height and wind speed with good accuracy could have significant impact when quick and reliable information concerning sea state is desired.

Acknowledgments. The authors would like to thank John R. Apel, NOAA/PMEL; William J. Campbell, Ice Dynamics Project, USGS; Edward Christensen of JPL; and Norbert Lannelongue of CNES for their help in the various stages of the research leading to this paper.

REFERENCES

Barrick, D. E., Wind dependence of quasi-specular microwave sea scatter, *IEEE Trans. Antennas Propagat.*, AP-22, 135-136, 1974.
 Brown, G. S. (Ed.), Skylab S-193 radar altimeter experiment analyses and results, chap. 6, *NASA Contract. Rep.*, CR-2763, 1977.
 Brown, G. S., Correlation of $\sigma^0(0^\circ)$ inferred wind speed estimates with NOAA hindcast data, *NASA Contract. Rep.*, CR-141437, 1978.
 Brown, G. S., and W. J. Curry, The estimation of pointing angle and σ^0 from Geos-3 radar altimeter measurements, *NASA Contract. Rep.*, CR-141426, 1977.
 Cox, C., and W. Munk, Measurement of the roughness of the sea surface from photographs of the sun's glitter, *J. Opt. Soc. Amer.*, 44, 838-850, 1954.
 Fedor, L. S., and D. E. Barrick, Measurement of ocean wave heights with a satellite radar altimeter, *Eos Trans. AGU*, 59, 843, 1978.
 Gower, J. F. R., The computation of ocean wave heights from Geos 3 satellite radar altimeter data, *Remote Sensing Environ.*, in press, 1978.
 Hammond, D. L., R. A. Mennella, and E. J. Walsh, Short pulse radar used to measure sea surface wind speed and SWH, *IEEE Trans. Antennas Propagat.*, AP-25(1), 61-67, 1977.
 Hayne, G. S., Initial development of a method of significant wave heights estimation for Geos 3, *NASA Rep. NAS6-2520*, Aug. 1977.
 Leitao, C. D., C. L. Purdy, R. L. Brooks, Wallops Geos C altimeter preprocessing report, *NASA Rep. NAS6-2173*, Feb. 1974.
 Longuet-Higgins, M. S., On the statistical distribution of the heights of sea waves, *J. Mar. Res.*, 11, 245-266, 1952.
 Matthews, R. E. (Ed.), Active microwave workshop report, *NASA Spec. Publ.*, SP-376, 171-172, 1975.
 McGoogan, J. T., Satellite altimetry applications, *IEEE Trans. Microwave Theory Tech.*, MTT-23(12), 970-978, 1975.
 McMillan, J. D., and N. A. Roy, A comparison of Geos 3 significant

TABLE 1. Frequency Distribution of Residuals

	1σ	2σ	3σ	Total
	38	45	45	46
	83%	98%	98%	
	18	25	28	28
	64%	89%	100%	
	5	10	11	11
	45%	91%	100%	
	51	80	84	85
	60%	94%	99%	

$\Delta U_1 = U_{gsp} - U_{AGC}$

	1σ	2σ	3σ	Total
(a)	19	28	33	35
	54%	80%	94%	
(b)	17	25	30	32
	53%	78%	94%	
(c)	4	10	13	14
	29%	71%	93%	
Total	40	63	76	81
	49%	78%	94%	

$\Delta U_2 = U_{ship} - U_{AGC}$

- wave height and wind speed data with National Buoy data, paper presented at the Geos 3 Final Review Meeting, NASA, New Orleans, La., November 1977.
- Miller, L. S., and G. S. Hayne, Characteristics of ocean reflected short radar pulses with application to altimetry and surface roughness determination, in *Sea Surface Topography from Space*, vol. 1, edited by J. Apel, p. 12, U.S. Government Printing Office, Washington, D. C., 1972.
- Miller, L. S., G. S. Hayne, and G. S. Brown, Analysis of satellite altimeter signal characteristics and investigation of sea-truth data requirements, *NASA Rep. NAS6-1952*, April 1972.
- Parsons, C. L., The measurement of significant wave height in near real-time using Geos-3 radar altimeter (abstract), *Eos Trans. AGU*, 87, 944, 1976.
- Pierson, W. J., and R. E. Salfi, Verification results for the spectral ocean wave model (SOWM) by means of significant wave height measurements made by the Geos 3 spacecraft, *NASA Contract Rep., CR-62089*, 1978.
- Rufenach, C. L., and W. R. Alpers, Measurement of ocean wave heights using the Geos 3 altimeter, *J. Geophys. Res.* 83(C10), 5011-5018, 1978.
- Skolnik, M., *Radar Handbook*, McGraw-Hill, New York, 1970.

(Received January 1, 1978;
revised December 18, 1978;
accepted January 3, 1979.)